A fusion approach to unconstrained iris recognition

Gil Santos [a,*], Edmundo Hoyle [b]

[a] Department of Computer Science, IT – Instituto de Telecomunicações, University of Beira Interior, Covilhã, Portugal
[b] Department of Electrical Engineering, Federal University of Rio de Janeiro, Rio de Janeiro, Brazil

ARTICLE INFO

ABSTRACT

As biometrics has evolved, the iris has remained a preferred trait because its uniqueness, lifetime stability and regular shape contribute to good segmentation and recognition performance. However, commercially deployed systems are characterized by strong acquisition constraints based on active subject cooperation, which is not always achievable or even reasonable for extensive deployment in everyday scenarios. Research on new techniques has been focused on lowering these constraints without significantly impacting performance while increasing system usability, and new approaches have rapidly emerged. Here we propose a novel fusion of different recognition approaches and describe how it can contribute to more reliable noncooperative iris recognition by compensating for degraded images captured in less constrained acquisition setups and protocols under visible wavelengths and varying lighting conditions. The proposed method was tested at the NICE.II (Noisy Iris Challenge Evaluation – Part 2) contest, and its performance was corroborated by a third-place finish.

© 2011 Elsevier B.V. All rights reserved.

1. Introduction

The use of the iris as main biometric trait has emerged as one of the most recommended methods due not only to the possibility of noncontact data acquisition and to its circular and planar shape that facilitates detection, segmentation and compensation for off-angle capture but also for its predominately randotypic appearance. Although these factors contribute to high effectiveness in the currently deployed iris-recognition systems, their typical scenarios are quite constrained: subjects stop and stare relatively close to the acquisition device while their eyes are illuminated by a near-infrared light source, enabling the acquisition of high-quality data. As reported in the study conducted by *Aton Origin* for the United Kingdom Passport Service,[1] imaging constraints are a major obstacle for the mass implementation of iris-based biometric systems. Notably, several researchers are currently working on minimizing the constraints associated with this process, in a way often referred to as noncooperative iris recognition, referring to several factors that can make iris images nonideal, such as at-a-distance imagery, on-the-move subjects, and high dynamic lighting variations.

In this study, we stress multiple recognition techniques, each one based on a different rationale and exploiting different properties of the eye region. Furthermore, we show how their fusion can increase the robustness to the degraded data typically captured in unconstrained acquisition setups.

The recognition techniques used in our proposition can be divide in two main categories. In one approach, we use wavelet-based iris-feature-extraction methods, complemented with a zero-crossing representation (Hoyle et al., 2010, 2009) and the analysis of iriscode-matching bit distribution (Santos and Proença, 2010). Complementarily, we expanded the extraction of features to the ocular region outside the iris, as recent studies (Savvides et al., 2010; Miller et al., 2010; Park et al., 2009) have suggested using these data, which appear to be a middle ground between iris and face biometrics and incorporates some advantages of each.

The performance of the fusion method we propose is highlighted by its third-place finish at the NICE.II (Noisy Iris Challenge Evaluation – Part 2), an international contest involving almost seventy participants worldwide.

The remainder of this paper is structured as follows: Section 2 describes the steps for iris-boundary localization and normalization, feature extraction and matching for the different approaches, and how their outputs are joined; Section 3 details the experimental process followed by a discussion of the obtained results; finally, Section 4 states the conclusions.

2. Proposed methodology

This section describes the five steps of our approach: iris-boundary detection, iris normalization, feature extraction, matching and decision ensemble (as schematized in Fig. 1). Furthermore, for feature extraction and matching, five recognition techniques are detailed.

---

* Corresponding author. Tel.: +351 92 683 24 68.
 E-mail addresses: gmelfe@ubi.pt (G. Santos), edhoyle@pads.ufrj.br (E. Hoyle).
 [1] http://www.ips.gov.uk/cps/rde/xchg/ips_live/hs.xsl/publications.htm.
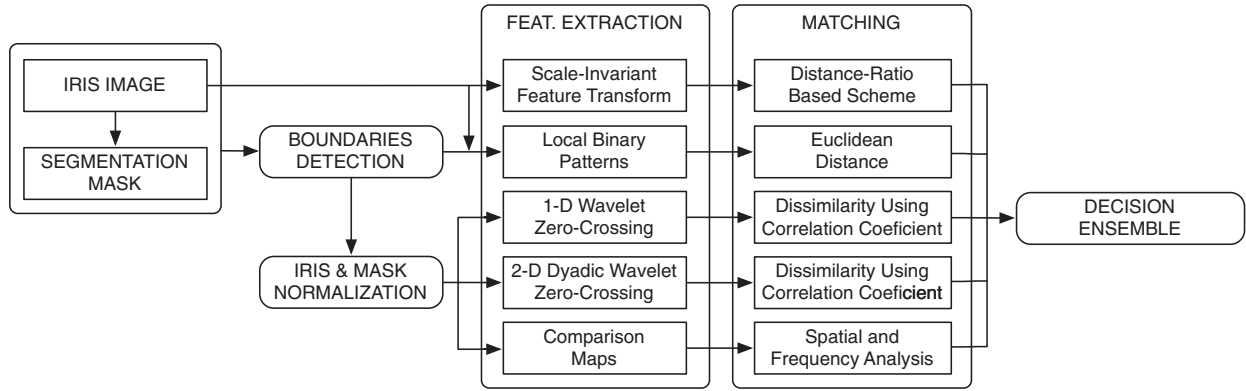
Fig. 1. Proposed methodology.

2.1. Iris boundaries detection

The first task was to locate the circles that best approximate iris and pupil boundaries, a necessity in the majority of methods used for this work. To accomplish this, we utilized a binary mask representing only parts containing iris information, created using the method proposed by Tan et al. (2010), winner of the NICE.I contest.

The steps taken in boundary approximation (Fig. 2(h)) were as follows:

- A contour is extracted from the segmentation mask Fig. 2(b), created with Tan et al. method (Tan et al., 2010). A pixel is part of such contour if it is nonzero, and connected to at least one zero-valued pixel.
- From the contour Fig. 2(c) of the segmentation mask Fig. 2(b), a Hough transform (Ballard, 1981) is applied to obtain the circle best fitting the iris Fig. 2(d).
- Convert the eye image Fig. 2(a) to grayscale and enhance it through histogram equalization Fig. 2(e).
- To the enhanced image Fig. 2(e), a Canny edge detection (Canny, 1986) is applied inside the circular region Fig. 2(f) concentric with the iris and 2/3 its radius, producing the edges shown in subFig. 2(g).
- Finally, a Hough transform is used on the resulting edge map Fig. 2(g) to obtain the circle that best fits the pupil.

Although this method produces good iris-boundary approximations, the estimated pupil limits sometimes diverge from ideal contours (e.g. Fig. 3). The main reason for this occurrence is poor lighting conditions when imaging heavily pigmented irises, which results in a low contrast ratio between the iris and the pupil.

2.2. Iris normalization

The iris-normalization process aims to obtain invariance with respect to size, position and pupil dilatation in the segmented iris region, which is accomplished by assigning each pixel to a pair of real coordinates (r, θ) over the double dimensionless pseudopolar coordinate system. For this purpose, we proceeded with the rubber-sheet model originally proposed by Daugman (2004).

$$I(x(r, \theta), y(r, \theta)) \rightarrow I(r, \theta) \qquad (1)$$

$$x(r, \theta) = (1 - r)x_p(\theta) + rx_s(\theta)$$
$$y(r, \theta) = (1 - r)y_p(\theta) + ry_s(\theta) \qquad (2)$$

where r and θ denote the radius and the angle, respectively, and $x(r, \theta)$ and $y(r, \theta)$ are defined as linear combinations of both the set of pupillary boundary points $(x_p(\theta), y_p(\theta))$ and the set of limbus
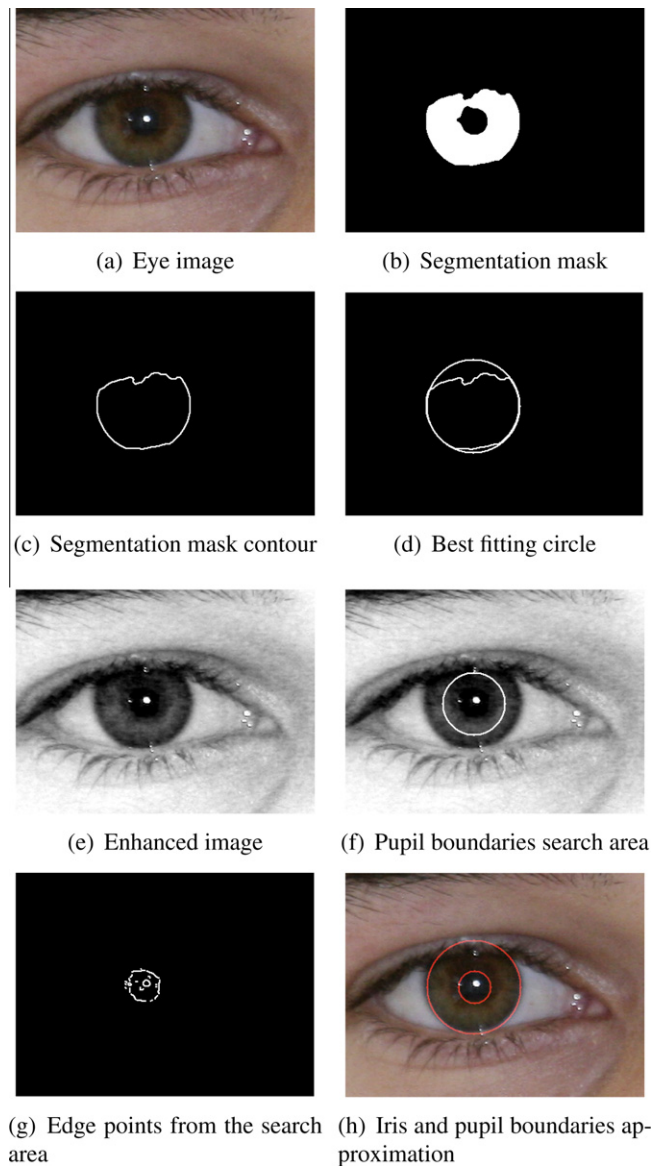

(a) Eye image   (b) Segmentation mask

(c) Segmentation mask contour   (d) Best fitting circle

(e) Enhanced image   (f) Pupil boundaries search area

(g) Edge points from the search area   (h) Iris and pupil boundaries approximation

Fig. 2. Illustration of the steps taken during the segmentation stage.

boundary points along the outer perimeter of the iris $(x_s(\theta), y_s(\theta))$ bordering the sclera.

Eqs. (1) and (2) give a transformation similar to that depicted in Fig. 4: subfigure (a) is the normalized iris image; subfigure (b)
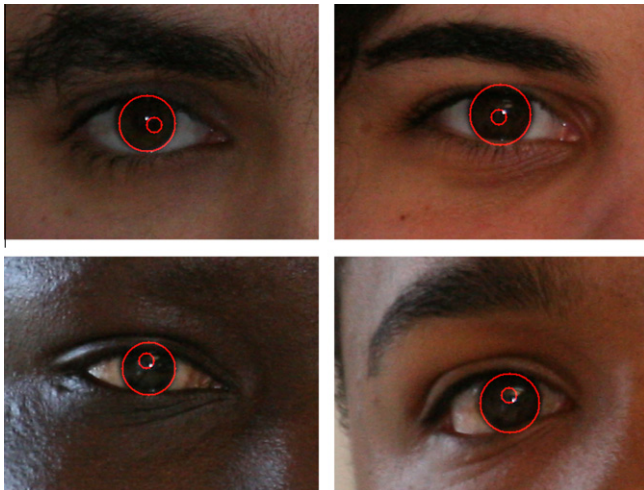
Fig. 3. Illustration of unsuccessful inner boundary detection.

(a) Normalized iris image

(b) Normalized segmentation mask

(c) Normalized iris image with occlusion zeroed

Fig. 4. Normalized images. Iris data are represented in grayscale.

represents the normalization of its mask (occlusions being the black region); and subfigure (c) is the normalized iris image where the occlusion has been zeroed. In either case, no interpolation was used, being chosen the nearest pixel to fill eventual gaps.

2.3. Feature extraction

Feature extraction and representation varies according to the employed method, as detailed herein.

2.3.1. 1-D wavelet zero-crossing representation

The representation method applied here is an extension of the Boles method (Boles and Boashash, 1998; Boles, 1997). Other studies (Hoyle et al., 2010, 2009) have shown that the proposed extension significantly improves the recognition performance.

The starting point for iris representation is the pixel-intensity data for the normalized iris image. In this representation, two normalized images are analyzed – with and without zeroed occlusion – as shown in the Fig. 4. Each row of the normalized images forms a vector which is later treated as a single-period sample of a one-dimensional periodic signal. A 1-D Gaussian wavelet transform (Daubechies, 1992) is applied to each row vector and decomposed into different resolution levels. The zero-crossing representation is then calculated for each row and resolution level. Zero crossings
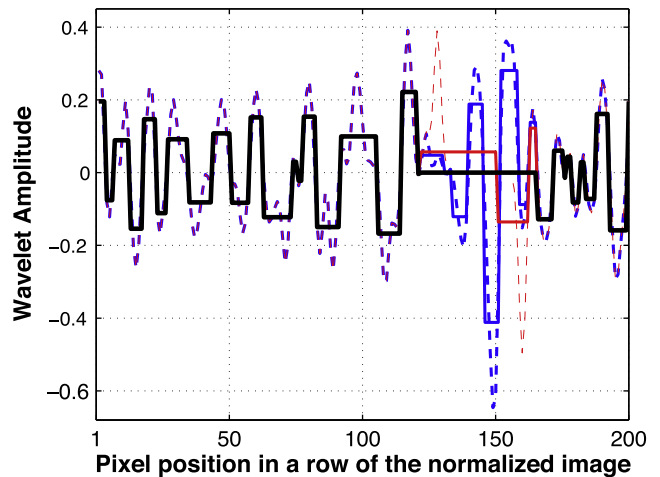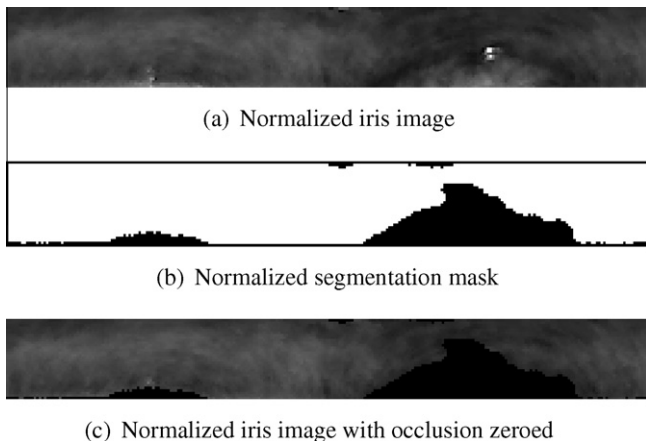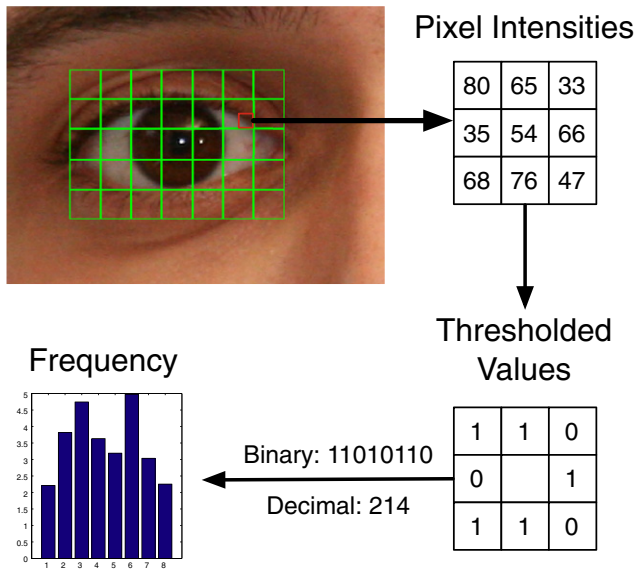

Fig. 5. Wavelet and zero-crossing representations.

occur where wavelet signals have abrupt changes in signal amplitude. Once the zero-crossings have been located, the average value between each two consecutive zero-crossing points in the wavelet output is computed.

Illustrated in Fig. 5 are wavelets for one resolution level (blue[2] and red dashed lines) and the respective zero-crossing representation (blue and red solid lines) from the same row of both the normalized iris (blue) and zeroed image (red), as well as the final zero-crossing representation (black line). As shown here, these wavelets (and their respective zero-crossing representations) differ at the regions where occlusion has been identified (the zeroed image). The final representation (black solid line in Fig. 5) is produced by starting from the zero-crossing representation (solid blue line) of the normalized iris image (Fig. 4(a)) and zeroing where it differs from the image (red solid line) for which occlusion was considered (Fig. 4(c)).

The values from the black solid line used in the iris representation were extracted from a 200×16 pixels normalized iris image, decomposed into three resolution levels (2, 3 and 4) for each row, resulting in a matrix of 48 rows by 200 columns.

2.3.2. 2-D dyadic wavelet zero-crossing representation

The earlier representation method used a 1-D Gaussian wavelet transform for each row of the normalized iris image. Here, a 2-D Daubechies dyadic wavelet transform (Daubechies, 1992) is applied instead.

To extract features from the normalized iris image, it is first convolved with a 2-D dyadic wavelet low-pass filter, minus the estimated value of both normalized iris images (Figs. 4(a) and (c)).

The resulting information matrices are then processed using the same technique for each row as detailed in Section 2.3.1, to obtain the final zero-crossing representation (Fig. 5 – black line) and represent the iris in a 200×16 matrix.

2.3.3. Periocular

New trends in biometrics (Park et al., 2009; Woodard et al., 2010) suggest the use of periocular information as an important addition in noncooperative biometric recognition, as information derived from this area is less prone to degradation in visible wavelengths than other traits (e.g., the iris). Representing a tradeoff between facial and iris recognition techniques, this method has the advantage of not requiring any additional equipment, as usually

---

[2] For interpretation of color in Figs. 4 and 5, the reader is referred to the web version of this article.

Fig. 6. Steps for LBP feature extraction.

such information is not discarded in iris databases. This technique is also less vulnerable to problems resulting from a lack of proper illumination or low-resolution acquisition, motion blur and varying imaging distances.

For the purpose of this work, we used the simple yet effective analysis suggested by Park et al. (2009).

Distribution-based descriptors. The iris location and size being known, images were aligned and normalized for both scale and translation as a set of regions of interest (Fig. 6) were defined according to those parameters. As shown here, iris size is proportional to the sides of each square region, and the central one is concentric with the iris itself.

Local Binary Pattern Pietikainen (2005) descriptors were then extracted, as depicted in Fig. 6. Using pixel intensities in a square window iterated over the entire region of interest, the difference between the central pixel and its eight neighbors was computed and its signal used to produce a binary result (thresholded values). Converting those results to decimal, values from each region were then quantized into eight-bin histograms, which upon concatenation produce the complete 280-feature array (35 regions × 8 bins per region).

Scale-Invariant Feature Transform. Differing from the previous method, where features were only extracted from the region closest to the eye, the Scale-Invariant Feature Transform (SIFT) (Lowe, 2004) was applied to all available data, here seeking salient regions (e.g., facial marks). SIFT is one of the most popular descriptors for image point matching, as it can achieve invariance to scale and rotation and is also robust to affine distortion. The method is based on the extraction of key points represented by vectors containing scale, orientation and location information. To achieve those results, a publicly available SIFT implementation[3] was used, and its parameters optimized based on tests performed on the training dataset.

2.3.4. Comparison maps

This approach (Santos and Proença, 2010) can be regarded as an extension to the widely known Daugman method (Daugman, 2004), which is the most widely acknowledged, with great acceptance over the scientific community.

---

[3] VLFeat open-source library http://www.vlfeat.org/.

This method begins with the detection and segmentation of the iris. For our approach, we used the procedures detailed above for the iris-boundary detection and normalization, except for the normalized iris sizes, which were 450×64 pixels for both the iris (Fig. 4(a)) and the noise mask (Fig. 4(b)).

Later, features were extracted through the convolution of the normalized data with a bank of 2-D Gabor wavelets, followed by a quantization stage that produced a binary *iriscode*, in which every complex-valued bit $h_{\{Re,Im\}}$ depends on the sign of the 2-D integral.

We decided on the use of a very small yet optimized wavelet bank, for which performance was optimized using the training data. For such optimization, we parameterized the wavelets cycling through a range of scales, orientations and frequencies we found fit, searching for the configuration that maximized the decidability (13).

2.4. Matching

In this section, the matching process is described for each one of the feature-extraction methods.

2.4.1. 1-D and 2-D wavelet zero-crossing representation

To compute the dissimilarity between two irises, their zero-crossing representations are compared. Boles (1997) proposed four functions to measure the dissimilarity between the signals. In this work, we used the dissimilarity measure defined by Eq. (3).

$$d_{lm}(f,g) = 1 - \frac{\sum_{e=0}^{E-1} Z_l f(e) \cdot Z_l g(e+m)}{\|Z_l f\| \|Z_l g\|} \tag{3}$$

In the above equation, $d_{lm}(f,g)$ denotes the dissimilarity of irises f and g associated with the lth row of their representation matrices for a displacement m, the vectors $Z_l f$ and $Z_l g$ are the lth row of the zero-crossing representations of irises f and g, respectively, E is the number of elements of $Z_l f$ and $Z_l g$ and $m, e \in [0, E-1]$. The symbol $\| \cdot \|$ denotes the vector-norm operation. Note that $d_{lm}(f,g)$ is equal to 1 minus the correlation coefficient between $Z_l f(e)$ and $Z_l g(e)$. Thus the dissimilarity $d_{lm}(f,g)$ may take values between 0 and 2, whereby 0 corresponds to a perfect match.

Eq. (3) is computed for each row of the representation matrices and determine which mean is taken as the dissimilarity (D_m) between irises f and g for a given value of m.

This work proposes the use of a weighted mean rather than a simple mean, whereby the weights are given by the number of nonzeroed values in $Z_j f(n)$ and $Z_j g(n)$ according to:

$$D_m = \frac{\sum_{l=1}^{L} d_{lm}(f,g) \times K_l}{\sum_{l=1}^{L} K_l} \tag{4}$$

where $d_{lm}(f,g)$ is given by (3) and K_l is the number of nonzeroed values in the lth row of the zero-crossing representations of both images.

It is important to notice that m in Eq. (3) represents the shifts of the second signal. Varying m in (3) from 0 to $E-1$ yields E dissimilarity values (D_m). The overall dissimilarity D between irises f and g is given by:

$$D = \min(D_m) \tag{5}$$

2.4.2. Periocular

From periocular analysis, two types of results were produced.

To compute the matching between two feature vectors u and v with n elements produced by the distribution-based descriptor, we used a Euclidean distance (6):

(a) Iriscode match sample

(b) Iriscode match with high concordance (de
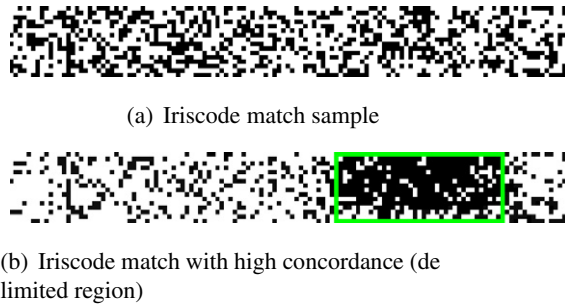limited region)

Fig. 7. Illustration of two iriscode matching results. Black pixels express concordant bits in the correspondent biometric signatures.

$$d(u,v) = \sqrt{\sum_{i=1}^{n}(u_i - v_i)^2} \qquad (6)$$

As for the features extracted by the SIFT, the distance-ratio-based matching scheme (Lowe, 2004) was applied.

2.4.3. Comparison maps

With two binary codes (*codeA* and *codeB*) and the corresponding segmentation masks (*maskA* and *maskB*), the *Hamming* distance (8) is applied as comparison measure.

$$c = (codeA \otimes codeB) \cap maskA \cap maskB \qquad (7)$$

$$HD = \frac{\|c\|}{\|maskA \cap maskB\|} \qquad (8)$$

where $\otimes$ is the logical XOR operation, $\cap$ is the logical AND and c is the "comparison map".

Instead of using the Hamming Distance alone (which is simply the ratio of concordant iriscode bits) as a single comparison measure, the resulting "comparison maps" (Fig. 7(a) and Eq. (7)) from the similarity between iriscodes are then subjected to both spatial and frequency-domain analysis in a search for high-concordance areas (Fig. 7(b)).

Spatial-domain analysis. For the spatial-domain analysis, we proceeded with a set of convolutions with Haar-based wavelets of different sizes, which allowed us to ascertain the concordance level of regions with different sizes.

Let c be a *comparison map* of $M \times N$ dimensions. Let h be a Haar-based mother wavelet with size $s \times s$. The similarity r in local regions of c is given by:

$$r_s = h_s * c, \quad s = \{2k\}, \quad k = 2, 3, \ldots, 16 \qquad (9)$$

where $*$ denotes the bidimensional convolution and r_s has the same dimensions of c.

Let $\omega_s = \max\{r_s(i,j)\}$, $i = 1, 2, \ldots, N$; $j = 1, 2, \ldots, M$.

Let H be the 25-bin histogram of $r_{\frac{\psi}{2}}$ where ψ is the maximum size of the Haar-wavelet, such that $H = \{h_1, h_2, \ldots, h_{25}\}$.

Using ω_i and h_i values, features were produced and used as detailed in the Classification subsection.

Frequency-domain analysis. For the frequency-domain analysis, the Fourier transform F of the comparison map c of $M \times N$ dimensions was computed as follows:

$$F(u,v) = \frac{1}{N}\sum_{x=0}^{M}\sum_{y=0}^{N}c(x,y)e^{-j2\pi(ux/M + vy/N)} \qquad (10)$$

where j is the square root of -1 and e denotes the natural exponent.

The results were then regularly windowed in sixteen subregions, and statistical features were extracted from each region. For the central part, where the most relevant information lies, we considered a $P \times N$ window centered in the $P \times M$ matrix that contains the noticeable central shape such that $P = 2M/8$. Ten features F_i are then extracted, representing the distribution of an evenly spaced ten-bin histogram:

$$T_i = \min(A) + i\frac{\Delta A}{10} \qquad (11a)$$

$$F_i = \sum_{m=1}^{P}\sum_{n=1}^{N} sgn(A_{(m,n)} - T_i) \qquad (11b)$$

with $\Delta A = \max(A) - \min(A)$ and $i = 1, 2, \ldots, 10$.

Classification. Combining the best features (according to their individual decidability) and performing a dimensionality reduction through Local Fisher Discriminant Analysis (Sugiyama, 2006), a logistic regression (Hosmer and Lemeshow, 2000) was used to describe the function that eventually produced the final result for this method.

2.5. Decision ensemble

With several outputs coming from the different representation methodologies, a logistic regression model (Agresti, 2002; Cantor, 2002; Hosmer and Lemeshow, 2000) was used to describe the relationship between them and a final response. This weight fitting methodology efficiency was verified on identical situations, with multiple classifiers of different accuracies (Monwar and Gavrilova, 2008, 2009; Santos and Proença, 2010).

The way this logistic regression works is equivalent to a single-output neural network with a logistic-activation function trained under log loss; this model is described by Eq. (12):

$$\log\left(\frac{p}{1-p}\right) = \beta_0 + \beta_1 x_1 + \beta_2 x_2 + \cdots + \beta_5 x_5 \qquad (12)$$

where the fraction $p/(1 - p)$ is called *the odds* of a positive match, that is, the ratio between that probability and its complementary. The β_i value is the weight relating the outputs x_i from the previously described methods to the odds.

3. Analysis of results

To assess the performance of the proposed method, experiments were conducted using 1,000 iris images from the UBIRIS.v2 (Proença et al., 2010) database used for the NICE.II[4] contest, and their respective segmentation masks. Although this contest was based only on identification mode (performance was ranked through the decidability measure), our experiments were carried out in two modes: verification mode (one-to-one matching) and identification mode (one-to-many matching).

In verification mode, we selected the well-known receiver-operating characteristic curves (ROC), the area under curve (AUC), the equal-error rate (EER) and the decidability (Daugman and Williams, 1996) index, given by Eq. (13):

$$d' = \frac{|\mu_{inter} - \mu_{intra}|}{\sqrt{\frac{\sigma_{inter}^2 + \sigma_{intra}^2}{2}}} \qquad (13)$$

where μ_{inter} and μ_{intra} denotes the means of the interclass and intraclass comparisons and σ_{inter} and σ_{intra} are the respective standard deviations.

The ROC curve is a graphical plot of the sensitivity, or true positive rate vs. false positive rate. The AUC can be perceived as a measure based on pairwise comparisons between classifications of two classes. With a perfect ranking, all positive examples are ranked higher than the negative ones and the area equal to 1. Any deviation from this ranking decreases the AUC. The EER of a

---

[4] NICE.II - http://www.nice2.di.ubi.pt.

Table 1
Recognition rates of each test.

	DEC	EER (%)	AUC
LBP	0.99	31.87	0.76
SIFT	0.87	32.09	0.74
1-D wavelet	1.44	23.12	0.85
2-D wavelet	1.29	25.04	0.82
Comparison maps	1.27	24.99	0.82
Fusion	1.74	18.48	0.90

Fig. 9. CMC curves for all matchers and their fusion.
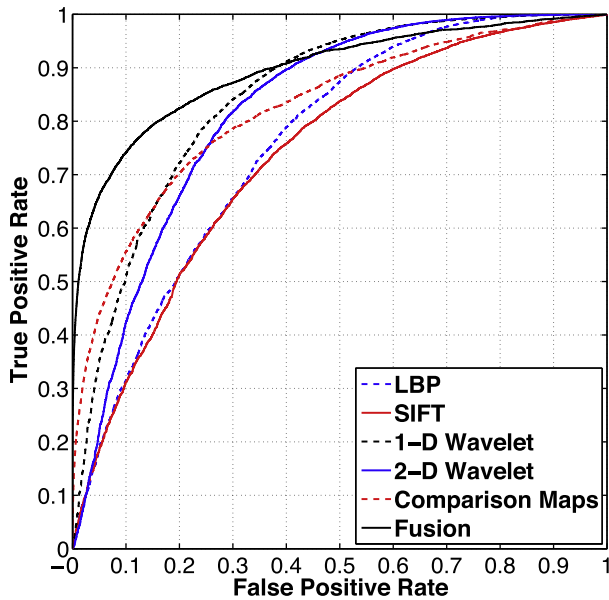
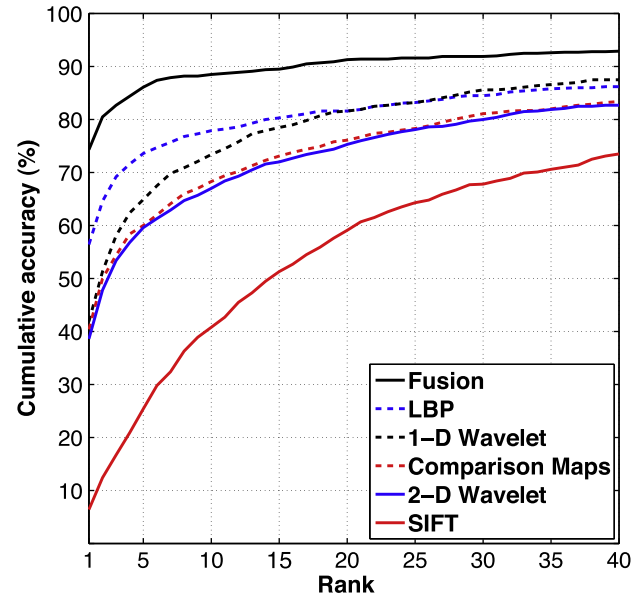**Fig. 8.** ROC curves for all matchers and their fusion.

verification system means that the operating threshold for the accept/reject decision is adjusted so that the probability of false acceptance and false rejection becomes equal.

In identification mode, where a subject is matched against a database in a 1:*N* way, a good performance assessment is the Cumulative Match Characteristic (CMC), as it shows the identification probability against the *N* closest candidates.

The parameters specified in the method description were tuned for best performance; here we chose those with maximal decidability indices, *i.e.*, those that maximize the average distance between distributions obtained for the two classical types of biometric comparisons: data extracted from the same (*intraclass*) and different eyes (*interclass*).

When applying the described methods independently on the training dataset, we obtained the results presented in Table 1 and Figs. 8 and 9.

As shown in Table 1, with respect to decidability (which was the criterion under consideration for the NICE.II contest), the best individual results were with the 1-D and 2-D Wavelet methods, with decidability (DEC) values of 1.44 and 1.29, respectively, closely followed by comparison maps at 1.27. The same observation is valid for the AUC values, whereas for EER the comparison maps slightly outperform the 2-D wavelet. Periocular features, despite low individual performance, proved to be of great help when fused with the other methodologies. In fact, inspection of the CMC plot (Fig. 9), where the separability between intra- and interclass distributions is not as pronounced, shows that LBP is the best of all individual methods, with a 56.4% rank-1 cumulative accuracy *versus* the 41.9% of the 1-D wavelet, beaten only by the fusion, with a 74.3% rank-1 cumulative accuracy.
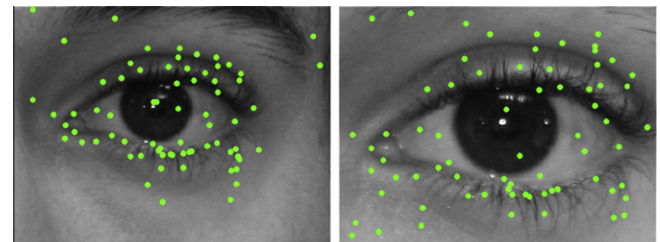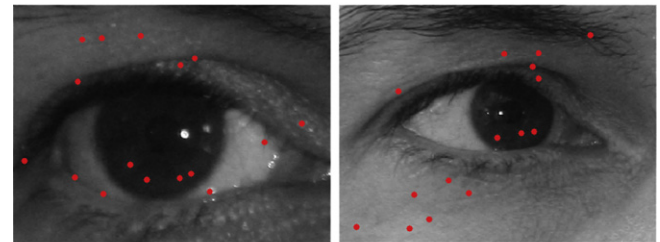
Fig. 10. SIFT performance examples in intraclass comparisons.

Fusing all the methods enhanced decidability to 1.74, representing an improvement of 20.8% over the best individual method. Improvements in identification performance were even more significant, as rank-1 was raised to 31.7%.

From these results, we can see that the entire method performance cannot be accessed by a single operational mode. We thus infer that, although some approaches improve recognition capabilities in verification scenarios, and some others work well for identification mode, their fusion produces more suitable outcomes, demonstrating the effectiveness of our method in both cases.

As the SIFT method uses more area for feature extraction than the others, it is more likely to be affected by strong variations in imaging conditions (*e.g.* pose or illumination; see Fig. 10(b)), thus producing globally unsatisfactory results. However, its good performance in some particular cases (*e.g.*, Fig. 10(a)) led us to include it, as its use improved the overall fused decidability by 4.5%.

4. Conclusions

In this study, we presented a novel fusion of different recognition approaches to address the issue of noncooperative iris recognition using nonideal visible-wavelength images captured in an unconstrained environment.

We tested several different autonomous approaches; their individual performances were evaluated in identification and verification modes and then the methods were fused, resulting in improved accuracy. We also showed that combining features extracted from the iris region itself with periocular information improves the overall performance in both recognition modalities.

The robustness of our approach was corroborated by independent evaluation in the NICE.II iris-recognition contest, where our method placed third rank among almost seventy participants from all over the world.

Acknowledgments

References

Agresti, A., 2002. Categorical Data Analysis (Wiley Series in Probability and Statistics). Wiley Interscience, Hoboken, NJ.

Ballard, D., 1981. Generalizing the Hough transform to detect arbitrary shapes. Pattern Recognition 13 (2), 111–122.

Boles, W., 1997. A security system based on human iris identification using wavelet transform. In: KES'97: Proc. First Internat. Conf. on Knowledge-Based Intelligent Electronic Systems, vol. 2, pp. 533–541.

Boles, W., Boashash, B., 1998. A human identification technique using images of the iris and wavelet transform. IEEE Trans. Signal Process. 46 (4), 1185–1188.

Canny, J., 1986. A computational approach to edge detection. IEEE Trans. Pattern Anal. Machine Intell. PAMI-8 (6), 679–698.

Cantor, A.B.M., 2002. Understanding logistic regression. Evidence-based Oncology 3 (2), 52–53.

Daubechies, I., 1992. Ten Lectures on Wavelets. SIAM.

Daugman, J.G., 2004. How iris recognition works. IEEE Trans. Circuits Systems Video Technol. 14 (1), 21–30.

Daugman, J., Williams, G., 1996. A proposed standard for biometric decidability. In: Proceedings of the CardTech/SecureTech Conf., pp. 223–234.

Hosmer, D.W., Lemeshow, S., 2000. Applied logistic regression (Wiley Series in probability and statistics). Wiley-Interscience Publication.

Hoyle, E., Feitosa, R., Petraglia, A., 2009. Iris recognition using one-dimensional signal analysis. In: Proc. 8th Internat. Seminar on Electrical Metrology.

Hoyle, E., Feitosa, R., Petraglia, A., 2010. VIII Semetro Book, EDUFCG: Editora da Universidade Federal de Campina Grande, 2010, pp. 141–161 (Chapter. 8: Robust Iris Segmentation for Biometric Recognition).

Lowe, D.G., 2004. Distinctive image features from scale-invariant keypoints. Internat. J. Comput. Vision 60, 91–110.

Miller, P.E., Rawls, A.W., Pundlik, S.J., Woodard, D.L., 2010. Personal identification using periocular skin texture. In: SAC'10: Proc. 2010 ACM Symp. on Applied Computing. ACM, New York, NY, USA, pp. 1496–1500.

Monwar, M., Gavrilova, M., 2008. FES: A system for combining face, ear and signature biometrics using rank level fusion. In: ITNG 2008: Fifth Internat. Conf. on Information Technology: New Generations, pp. 922–927.

Monwar, M., Gavrilova, M., 2009. Multimodal biometric system using rank-level fusion approach. IEEE Trans. Systems Man Cybernet. Part B: Cybernetics 39 (4), 867–878.

Park, U., Ross, A., Jain, A., 2009. Periocular biometrics in the visible spectrum: A feasibility study. In: BTAS'09: Proc. IEEE 3rd Internat. Conf. on Biometrics: Theory, Applications, and Systems, 2009, pp. 1–6.

Pietikainen, M., 2005. Image analysis with local binary patterns. In: Kalviainen, H., Parkkinen, J., Kaarna, A. (Eds.), Image Analysis, Lecture Notes in Computer Science, vol. 3540. Springer, Berlin/Heidelberg, pp. 115–118.

Proença, H., Filipe, S., Santos, R., Oliveira, J., Alexandre, L.A., 2010. The ubiris.v2: A database of visible wavelength iris images captured on-the-move and at-a-distance. IEEE Trans. Pattern Anal. Machine Intell. 32, 1529–1535.

Santos, G., Proença, H., 2010. Iris recognition: Analyzing the distribution of iriscodes concordant bits. In: CISP 2010: Proc. 3rd Internat. Congress on Image and Signal Processing, vol. 4, pp. 1873–1877.

Savvides, M., Ricanek Jr., K., Woodard, D.L., Dozier, G., 2010. Unconstrained biometric identification: Emerging technologies. Computer 43, 56–62.

Sugiyama, M., 2006. Local fisher discriminant analysis for supervised dimensionality reduction. In: ICML'06: Proc. 23rd Internat. Conf. on Machine Learning. ACM Press, New York, NY, USA, pp. 905–912.

Tan, T., He, Z., Sun, Z., 2010. Efficient and robust segmentation of noisy iris images for non-cooperative iris recognition. Image Vision Comput. 28 (2), 223–230.

Woodard, D., Pundlik, S., Miller, P., Jillela, R., Ross, A., 2010. On the fusion of periocular and iris biometrics in non-ideal imagery. In: ICPR 2010: Proc. 20th Internat. Conf. on Pattern Recognition, pp. 201–204.